RESEARCH ARTICLE
PLANETARY SCIENCES

Earth and Planetary Physics
9: 1147–1156, 2025
doi: 10.26464/epp2025084

Martian atmosphere sputtering escape generated by penetrating hydrogen energetic neutral atoms

JiJie Ma[1,2,3], LingGao Kong[4,1*], Hao Gu[5], WenYa Li[6], YuMing Wang[7,8], YuTian Chi[9], BinBin Tang[6], XiaoPeng Liu[2,6], YiFan Song[4], BaiQu Pu[4], FuHao Qiao[2,6], LiMin Wang[2,6], Jun Cui[5], Yong Wei[10], AiBing Zhang[1,2,3*], and Chi Wang[2,5]

[1]Beijing Key Laboratory of Space Environment Exploration, National Space Science Center, Chinese Academy of Sciences, Beijing 100190, China;

[2]University of Chinese Academy of Sciences, Beijing 101408, China;

[3]Key Laboratory of Science and Technology on Space Environment Awareness, Chinese Academy of Sciences, Beijing 100190, China;

[4]Institute of Science and Technology for Deep Space Exploration, Suzhou Campus, Nanjing University, Suzhou Jiangsu 215163, China;

[5]Planetary Environmental and Astrobiological Research Laboratory, School of Atmospheric Sciences, Sun Yat-Sen University, Zhuhai Guangdong 519000, China;

[6]State Key Laboratory of Solar Activity and Space Weather, National Space Science Center, Chinese Academy of Sciences, Beijing 100190, China;

[7]National Key Laboratory of Deep Space Exploration/School of Earth and Space Sciences, University of Science and Technology of China, Hefei 230026, China;

[8]Chinese Academy of Sciences (CAS) Center for Excellence in Comparative Planetology/CAS Key Laboratory of Geospace Environment/Mengcheng National Geophysical Observatory, University of Science and Technology of China, Hefei 230026, China;

[9]Institute of Deep Space Sciences, Deep Space Exploration Laboratory, Hefei 230088, China;

[10]Key Laboratory of Earth and Planetary Physics, Institute of Geology and Geophysics, Chinese Academy of Sciences, Beijing 100191, China

Key Points:

- The first direct dayside observations of penetrating hydrogen energetic neutral atoms (H-ENAs) at Mars have been obtained using Tianwen-1's MINPA (Mars Ion and Neutral Particle Analyzer) instrument.
- The estimated oxygen sputtered escape rate (5.5×10^{23} s^{-1} to 5.2×10^{24} s^{-1}) is comparable to or exceeds ion-driven escape rates observed by MAVEN (Mars Atmosphere and Volatile EvolutioN).
- The findings underscore the importance of low-altitude (approximately hundreds of kilometers) H-ENA observations to better constrain nonthermal escape processes and upper atmospheric interactions.

Citation: Ma, J. J., Kong, L. G., Gu, H., Li, W. Y., Wang, Y. M., Chi, Y. T., Tang, B. B., Liu, X. P., Song, Y. F., ... Wang, C. (2025). Martian atmosphere sputtering escape generated by penetrating hydrogen energetic neutral atoms. *Earth Planet. Phys.*, *9*(6), 1147–1156. http://doi.org/10.26464/epp2025084

Abstract: Atmospheric escape plays a critical role in shaping the long-term climate evolution of Mars. Among the various escape mechanisms, energetic neutral atoms (ENAs) generated through charge exchange between solar wind ions and exospheric neutrals serve as an important diagnostic for ion–neutral interactions and upper atmospheric loss. This study presents direct observations of hydrogen ENAs (H-ENAs) on the dayside of Mars by using the Mars Ion and Neutral Particle Analyzer (MINPA) onboard China's Tianwen-1 orbiter. By analyzing H-ENA data during a coronal mass ejection and a stream interaction region from December 29, 2021, to January 1, 2022, and comparing these data with MAVEN/SWIA (Mars Atmosphere and Volatile EvolutioN/Solar Wind Ion Analyzer) solar wind measurements, we examine the temporal evolution of H-ENA flux and the associated sputtered escape of atmospheric constituents. The observed H-ENA velocity is consistent with upstream solar wind ions, and the H-ENA-to-ion intensity ratio is used to infer variations in exospheric density, revealing a delayed response to enhanced solar wind activity. Penetrating H-ENA intensities reach up to 5.3×10^6 s^{-1} cm^{-2}, with energy fluxes on the order of $(0.5–8.1) \times 10^{-3}$ mW/m^2. The estimated oxygen sputtered escape rate driven by penetrating H-ENAs ranges from 5.5×10^{23} s^{-1} to 5.2×10^{24} s^{-1}, comparable to or exceeding previous estimates based on penetrating ions. The findings highlight the need for low-altitude H-ENA observations to better quantify their atmospheric interactions and refine our understanding of nonthermal escape processes at Mars.

Keywords: penetrating energetic neutral atoms; sputtered escape; Mars atmosphere loss; Tianwen-1; future energetic neutral atom observations

First author: J. J. Ma, majijie19@mails.ucas.ac.cn
Correspondence to: L. G. Kong, lgkong@nju.edu.cn
A. B. Zhang, zhab@nssc.ac.cn
Received 24 APR 2025; Accepted 19 MAY 2025.
First Published online 14 JUL 2025.
©2025 by Earth and Planetary Physics.

1. Introduction

Mars, the red planet, possesses lower gravity and a thinner atmosphere than Earth. Geological evidence suggests that Mars once experienced a warmer and wetter climate (Carr, 1986), implying

that the planet has undergone substantial atmospheric evolution, with a substantial fraction of its atmospheric constituents lost to space (Catling, 2009; Lammer et al., 2013; Lillis et al., 2015). Consequently, atmospheric escape processes are a key focus in Martian studies, offering critical insights into the planet's climatic and atmospheric evolution.

Multiple mechanisms contribute to atmospheric loss, including thermal (Jeans) escape, photochemical escape, and atmospheric sputtering for neutral particles, as well as ion outflows through the magnetotail, the ion plume, and pick-up processes for ionized particles (Lillis et al., 2015). The Mars Express (Schmidt, 2003) and the Mars Atmosphere and Volatile EvolutioN (MAVEN) missions (Jakosky et al., 2015) have provided extensive studies of these escape processes. For oxygen (O), a key factor in Mars' water loss, the total escape rate is given as 6×10^{25} s^{-1} (Jakosky et al., 2018), with photochemical escape contributing $(3.5–7)\times10^{25}$ s^{-1} (Lillis et al., 2017), ion escape contributing $(1.8–5)\times10^{24}s^{-1}$ (Brain et al., 2015), and sputtering by penetrating ions contributing 1×10^{24} s^{-1} (Leblanc et al., 2015, 2018).

Because of the absence of a global magnetic field (Acuña et al., 1998), Mars undergoes direct interaction between its atmosphere and the solar wind. This intense ion–neutral coupling gives rise to a highly dynamic and complex space environment, profoundly shaping the structure of the induced magnetosphere and enhancing the efficiency of atmospheric escape. A key outcome of this interaction is the generation of energetic neutral atoms (ENAs; Futaana et al., 2011) through charge exchange (CEX) between energetic ions and neutral exospheric particles. Consequently, ENAs serve as a vital diagnostic tool for investigating the interactions between neutral and charged particle populations and the driven escape process.

Because ENAs are electrically neutral, they are unaffected by electromagnetic fields and can pass through plasma boundaries—such as the bow shock and the magnetic pileup boundary—without deflection. As a result, they can penetrate into the Martian atmosphere while retaining the velocity and directional information of their parent ions. These particles, known as penetrating ENAs (Kallio and Barabash, 2001), provide an additional channel of energy and mass input into the dayside Martian atmosphere, contributing to processes such as the proton aurora (Deighan et al., 2018; Chaffin et al., 2022) and sputtered escape (Lillis et al., 2015) resulting from collisions with atmospheric constituents.

Research on penetrating ENAs began with simulation-based studies. A pioneering three-dimensional Monte Carlo model (Kallio and Barabash, 2001) provided the first analysis of the altitude profiles of penetrating hydrogen ENAs (H-ENAs) and their interactions with the Martian atmosphere under varying solar zenith angles (SZAs). Subsequent work by Kallio et al. (2006) predicted the H-ENA albedo on the Martian dayside and introduced a novel technique for extracting information on the properties of the planetary exosphere and atmosphere through observations of these penetrating particles.

Mars Express, equipped with the Analyzer of Space Plasmas and Energetic Atoms (ASPERA-3) instrument (Barabash et al., 2006), provided the first ENA observations around Mars and considerably advanced our understandings of ENAs on the nightside of Mars (Galli et al., 2006, 2008), which include identification of the ENA jet (Futaana et al., 2006b) and confirmation of the presence of the H-ENA albedo (Futaana et al., 2006a). However, because of the interference by solar extreme ultraviolet (EUV) radiation along the Sun–Mars direction, Mars Express did not provide a direct observation of penetrating H-ENAs.

Indirect observations of penetrating H-ENAs have been provided by the Solar Wind Ion Analyzer (SWIA) onboard MAVEN (Halekas et al., 2015b). The SWIA is primarily designed to measure solar wind ions and is capable of detecting secondary ionized penetrating H-ENAs at low altitudes (Halekas et al., 2015a). The intensities and speeds of the penetrating H-ENAs can be estimated by assuming the dynamic equilibrium between the CEX and electron stripping process at low altitudes in the Mars atmosphere (Halekas, 2017). However, because of the absence of direct observations, such analyses rely on several assumptions, resulting in significant uncertainties and limiting deeper investigation into their atmospheric interactions, such as sputtered escape driven by penetrating H-ENAs.

Tianwen-1 (Yan G et al., 2018), China's first Mars exploration mission, comprises an orbiter, a lander, and the Zhurong rover (Ye P et al., 2017). The mission was launched on July 23, 2020, and successfully entered a Martian orbit on February 10, 2021. The orbiter carries three payloads dedicated to the Martian space environment: the Mars Ion and Neutral Particle Analyzer (MINPA; Kong LG et al., 2020), the Mars Orbiter Magnetometer (MOMAG; Liu K et al., 2020), and the Mars Energetic Particle Analyzer (MEPA; Tang SW et al., 2020). The MINPA provides both ion and ENA measurements. The ENA unit of the MINPA covers an energy range from 45.5 eV to 4.3 keV, with a field of view of $360°\times9.7°$. Leveraging advanced EUV absorption techniques (Wang LM et al., 2023), the MINPA is capable of observing ENAs originating from the Sun direction, thereby enabling the detection of penetrating H-ENAs.

In this study, we investigate a coronal mass ejection (CME) event with a stream interaction region (SIR) event observed by Tianwen-1 from December 28, 2021, to January 1, 2022 (Chi YT et al., 2023), with the aim of assessing variations in penetrating H-ENA intensity under dynamic solar wind conditions and the associated atmospheric sputtering escape. The analysis integrates MINPA H-ENA observations with MAVEN/SWIA ion measurements, magnetic field ($\boldsymbol{B}$) observations from the MOMAG and the MAVEN magnetic field investigation (Connerney et al., 2015), and a test particle Monte Carlo model (Gu H et al., 2019).

2. H-ENA Observations

As of November 2021, the Tianwen-1 spacecraft entered its scientific observation phase, following an elliptical orbit of 243 × 10,760 km with an orbital period of approximately 7.1 hours. The MINPA operates in three modes—the default mode, the magnetotail mode, and the ionosphere mode—which are designed to detect ions and ENAs in different regions. The default mode, used for most of the orbit, and the magnetotail mode, activated near apoapsis, provide both ion and ENA measurements. The ionosphere mode, utilized near periapsis, enables only ion detection.

Figure 1 presents the orbits of the Tianwen-1 and MAVEN space-

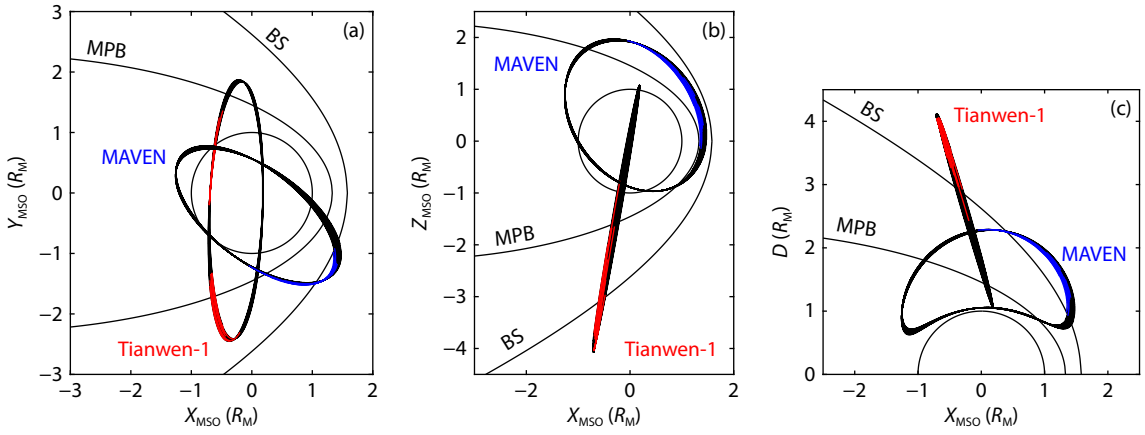

Figure 1. Tianwen-1 and MAVEN orbits from December 28, 2021, to January 1, 2022, in (a) *X*–*Y*, (b) *X*–*Z*, and (c) *X*–*D* $\left(D = \sqrt{Y^2 + Z^2}\right)$ planes. The locations of the nominal bow shock (BS) and magnetic pile-up boundary (MPB; Edberg et al., 2008) are also shown. The black curves represent the complete orbits, whereas the red and blue segments indicate the positions where Tianwen-1 and MAVEN were upstream of the BS. Here, we adopt the Mars–Sun orbital (MSO) coordinate system. R_M, Mars radii.

craft from December 28, 2021, to January 1, 2022. During this period, Tianwen-1's apoapsis was located in the southern hemisphere, with an SZA of 100°. This orbital configuration allowed the MINPA to observe H-ENAs both upstream of the bow shock and within the magnetospheric flanks. However, during periapsis observations on the Martian dayside, the MINPA was operated in the ionosphere mode, without ENA observations. The absence of low-altitude, low-SZA ENA data limits direct observations of dayside penetrating H-ENAs. Here, we use the high-altitude, large-SZA H-ENA measurements and an exosphere model to estimate the dayside penetrating H-ENA intensity.

The complexity and multiple origins of plasma downstream of the bow shock, along with its interactions with the neutral exosphere, result in a similarly complex and multi-origin composition of H-ENAs within the magnetosheath. These include H-ENAs originating from planetary H^+ (Lichtenegger et al., 2002) as well as from pristine and shocked solar wind ions (Holmström et al., 2002). Distinguishing these various ENA populations and isolating the penetrating H-ENAs are highly challenging. Therefore, this study focuses on observations upstream of the bow shock, where the H-ENA sources are more clearly identifiable. These H-ENAs are capable of travel through the bow shock and magnetic pile-up boundary before penetrating the Martian atmosphere. The red segments in Figure 1 indicate locations where Tianwen-1 was upstream of the bow shock, providing H-ENA observations. The MINPA provides ion measurements, and its solar wind ion observations during the Earth–Mars transfer phase show consistency with data from MAVEN, Mars Express, and the near-Earth OMNI dataset (Fan K et al., 2022; Zhang AB et al., 2022). However, because of the instrument's 2π field of view and attitude limitations during orbital operations, the MINPA may miss part of the solar wind ion distribution. Thus, we adopt the solar wind conditions from the MAVEN/SWIA data. The trajectories of MAVEN during the period investigated are also depicted in Figure 1, with the blue segments marking intervals when the spacecraft was located upstream of the bow shock. The nominal positions of the bow shock and magnetic pile-up boundary under average solar wind conditions (Edberg et al., 2008) are also shown in Figure 1.

Figure 2 presents the H-ENA, solar wind ion, and interplanetary magnetic field observations from MAVEN (Figures 2a–2d) and Tianwen-1 (Figures 2e–2h). Based on the interplanetary magnetic field data (Figures 2d and 2e) and the solar wind ion data (Figures 2a–2c), a CME impact on Mars is identified from 00:00 UTC (coordinated universal time) on December 29, 2021, to 20:00 UTC on December 30, 2021. This event is characterized by enhanced magnetic field strength, smooth rotation of the magnetic field vector, a gradual decrease in solar wind velocity, a low proton temperature, and reduced plasma beta, as detailed in Chi YT et al. (2023).

Prior to the CME, the average solar wind ion speed was approximately 385 km/s. During the early phase of the CME, the speed slightly decreased, ranging from 282 to 331 km/s, before an SIR impact at 05:00 UTC on December 30, 2021 (Chi YT et al., 2023), suggesting that Mars was initially situated within a low-speed solar wind region. Concurrently, the solar wind intensity gradually increased from 1.7×10^8 s^{-1} cm^{-2} at 02:10 UTC on December 30, 2021, to 5.7×10^8 s^{-1} cm^{-2} at 16:00 UTC on December 30, 2021, and remained at this level until approximately 03:00 UTC on December 31, 2021. Following this period, Mars transitioned into a high-speed solar wind region, with the ion bulk speed increasing to approximately 430 km/s. This was accompanied by a decline in solar wind intensity to approximately 1.9×10^8 s^{-1} cm^{-2}.

The H-ENA observations (Figures 2f–2h) provide an additional perspective on the influence of the CME and subsequent SIR on solar wind–Mars interactions. The H-ENA data obtained upstream of the bow shock (Figure 1) are used to trace CEX processes between the solar wind and the Martian exosphere and to infer exospheric variations in conjunction with upstream solar conditions. Figure 2f presents the energy-resolved H-ENA count rate spectrogram observed by the MINPA. Because of the low count rates of this H-ENA event, a 10-minute averaging window is applied to improve statistical reliability for subsequent analysis. The corresponding H-ENA intensity and speed, derived from the averaged spectra, are shown in Figures 2g and 2h, respectively.

Prior to the CME and during its initial phase (before 15:10 UTC),

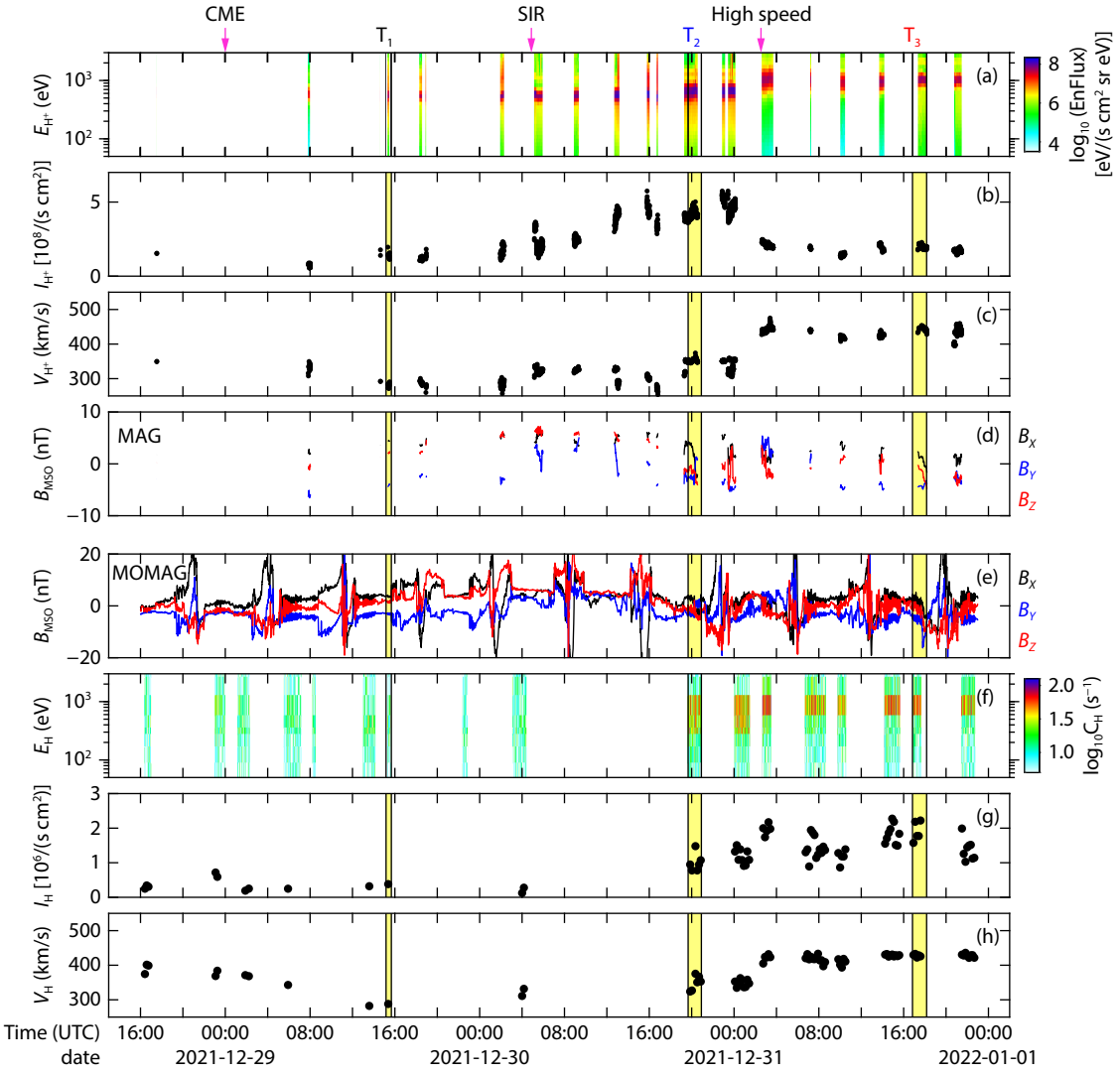

Figure 2. H-ENA and solar wind ion observations upstream of the bow shock during the CME impact on Mars from December 28, 2021, to January 1, 2022. (a) Solar wind ion differential energy flux spectrogram as a function of energy. (b) Intensity and (c) bulk speed of solar wind ions. (d) Magnetic field (***B***) in MSO coordinates observed by MAG. (e) ***B*** (thin curves) and ***B*** upstream of the bow shock (thick curves) in MSO coordinates observed by the MOMAG. The black, blue, and red curves in (d) and (e) show the *X*, *Y*, and *Z* components of ***B***. (f) H-ENA count rate spectrogram as a function of energy. (g) Intensity and (h) bulk speed of the H-ENAs. The yellow shading in panels (a) to (h) highlights the time intervals corresponding to the post-onset of the CME (15:10 to 15:40 UTC, T_1), the peak ion intensity (19:40 to 20:55 UTC, T_2), and the post-CME phase (16:50 to 18:10 UTC, T_3). Enflux = energy flux; C = count rate.

the H-ENA intensity (Figure 4g) remained relatively low, averaging 2.7×10^5 s^{-1} cm^{-2}, with particle velocities (Figure 4h) decreasing from 400 to 280 km/s—closely aligning with the solar wind ion speeds. At the onset of the CME (00:00 UTC on December 29), a distinct H-ENA intensity peak of 7.1×10^5 s^{-1} cm^{-2} was recorded. However, because of the absence of concurrent solar wind data and the lack of continuous H-ENA coverage during this period, it remains challenging to discern whether this enhancement resulted from an intensified solar wind ion flux or an increased exospheric density.

Following the arrival of the SIR, both the intensity and speed of H-ENAs increased, closely following the rise in solar wind bulk speed and ion flux. Notably, the H-ENA intensity peaked later than the solar wind ion intensity, reaching 2.1×10^6 s^{-1} cm^{-2} at 03:00 UTC on December 31—coinciding with the onset of the decline in ion flux. Thereafter, the H-ENA intensity remained elevated through January 1, 2022. The simultaneous increase in H-ENA intensity and decrease in solar wind ion flux (Figures 2g and 2b) suggests an enhancement in exospheric density during this interval.

To further investigate the effects of the CME and SIR on Mars, including their influence on the penetrating flux, energy, and sputtered escape, H-ENA and ion observation data from three characteristic intervals are analyzed: the post-onset of the CME (15:10 to 15:40 UTC, T_1), the peak ion intensity (19:40 to 20:55 UTC, T_2), and the post-CME phase (16:50 to 18:10 UTC, T_3). These intervals are marked by yellow shading in Figure 2. Figure 3 presents the time-averaged distribution of H-ENA differential particle flux as a function of energy and azimuthal angle during the three selected intervals. The circumferential direction denotes the azimuthal

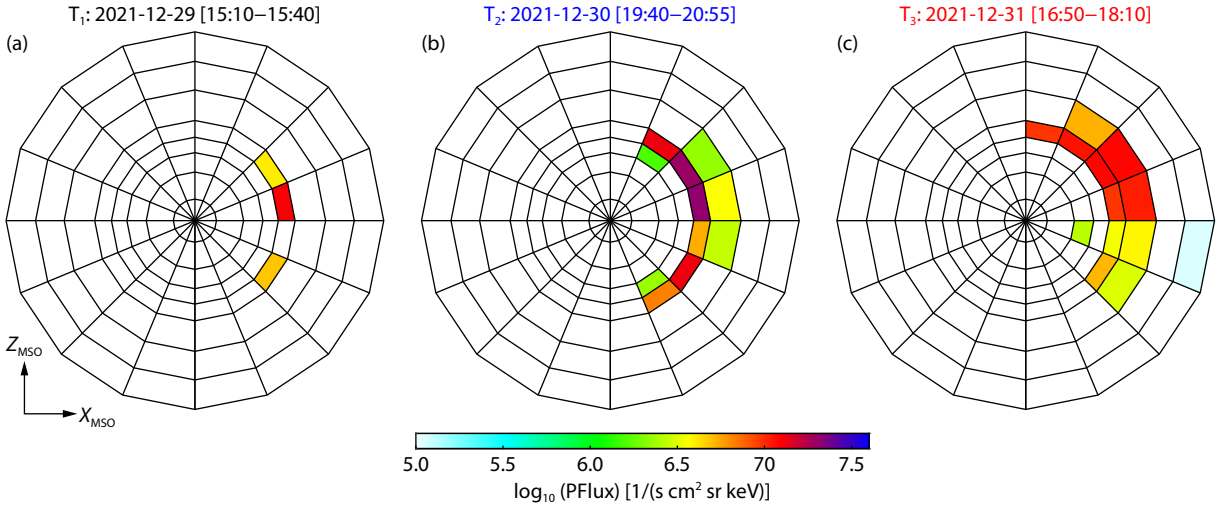

Figure 3. H-ENA differential particle flux in the *X*–*Z* plane at (a) T_1, (b) T_2, and (c) T_3. The radial ticks correspond to the eight energy channels at 46 eV, 97 eV, 168 eV, 269 eV, 421 eV, 859 eV, 1.9 keV, and 4.3 keV, and the circumferential ticks denote the 16 azimuth sectors of the MINPA.

angle of H-ENAs from 0° to 360° in the *X*–*Z* plane of the MSO coordinate system. The radial axis corresponds to the MINPA's H-ENA energy bins, with energies centered at 46 eV, 97 eV, 168 eV, 269 eV, 421 eV, 859 eV, 1.9 keV, and 4.3 keV. The colored pixels indicate the calculated differential particle flux at each energy–azimuth combination.

Figure 3a presents the H-ENA energy–angle distribution at the post-onset of the CME (T_1). During this interval, the distribution exhibits a low-energy peak at the energy bin centered around 421 eV, corresponding well with the solar wind ion bulk speed of 280 km/s (equivalent to 415 eV). By integrating the H-ENA differential particle flux over both the energy and azimuthal angle, the total H-ENA intensity is derived, as shown in Figure 2g. The average H-ENA intensity during T_1 is 3.8×10^5 s^{-1} cm^{-2}, with particles predominantly propagating along the $-X_{MSO}$ direction. The average intensity of solar wind ions during the same interval is 1.4×10^8 s^{-1} cm^{-2}, yielding a ratio of H-ENA to solar wind ion intensity of approximately 0.27%.

The H-ENA energy–angle distribution during the time interval of peak ion intensity (T_2), shown in Figure 3b, exhibits distinct characteristics compared with T_1. The H-ENA signal appears in the fourth and fifth energy bins, centered at 421 and 859 eV, indicating the presence of higher energy H-ENAs than at T_1. These energies correspond to a solar wind speed of approximately 351 km/s (equivalent to 643 eV). The average H-ENA intensity during T_2 is 1.0×10^6 s^{-1} cm^{-2}, which is significantly higher than that observed during T_1. The ratio of H-ENA to solar wind ion intensity (4.2×10^8 s^{-1} cm^{-2}) during T_2 is approximately 0.24%, comparable to the ratio during T_1. This similarity suggests that the exospheric density during T_2 remains at a level similar to that during T_1.

During T_3—the post-CME phase, when Mars is situated within the high-speed solar wind region—the H-ENAs exhibit higher energies (Figure 3c), consistent with the solar wind ion bulk speed of 440 km/s (1.02 keV). The H-ENA intensity during this interval increases significantly, reaching 1.9×10^6 s^{-1} cm^{-2}, whereas the solar wind ion intensity decreases to a relatively low level of 1.9×10^8 s^{-1} cm^{-2}. This shift results in a markedly higher H-ENA-to-solar wind ion intensity ratio of approximately 1%, indicating a substantially elevated exospheric density during T_3 compared with T_1 and T_2.

3. Atmospheric Sputtering Escape

From the H-ENA observations upstream of the bow shock, combined with the exosphere model, the H-ENA intensity at the dayside of Mars can be estimated. Here, we use the classical Chamberlain model (Chamberlain, 1963) to calculate the intensity of penetrating H-ENAs. In the Chamberlain model, the profile of the exosphere is defined by

$$n(r) = n_{exo}\times\exp\left(\lambda(r)-\lambda_{exo}\right)\times\zeta(\lambda), \tag{1}$$

$$\lambda(r) = \frac{GMm}{kT_{exo}r},\quad \lambda_{exo} = \lambda\left(r = r_{exo}\right). \tag{2}$$

Here, n and n_{exo} represent the number densities at the reference altitude and the exobase, respectively; r and r_{exo} are the distances from the center of Mars to the reference altitude and the exobase, respectively; T_{exo} is the temperature at the exobase; λ is the Jeans parameter; and ζ is the partition function as defined in Chamberlain (1963), which is a function of λ. In addition, G and k denote the gravitational constant and the Boltzmann constant, respectively, and M and m are the mass of Mars and the mass of exospheric particles, respectively.

The relationship between the intensity of ENAs at a reference position upstream of the bow shock and the solar wind ion intensity is described by the following equation:

$$I_H = \int_{LOS}\sigma\left(E_{H^+}\right)\cdot n(r)\cdot I_{H^+}\mathrm{d}r. \tag{3}$$

Here, σ is the CEX cross section for H–H$^+$ interactions, which depends on the particle energy and is provided by Lindsay and Stebbings (2005). The line of sight (LOS) extends from the reference position to infinity along the opposite direction of the incoming solar wind ions. Assuming that the solar wind ion intensity upstream of the bow shock is spatially uniform, Equation (3) simplifies to

$$I_H = I_{H^+} \cdot \sigma(E_{H^+}) \cdot \int_{LOS} n(r)\,dr. \quad (4)$$

Therefore, at a given time, the relative ENA intensities at different reference positions can be estimated based on the integrated exospheric density along the LOS.

According to the Chamberlain model, the exobase temperature (T_{exo}) governs the rate at which the exospheric density decreases with increasing distance from Mars. Therefore, given T_{exo}, the ratio between the H-ENA intensity at a specific position and the observed intensity can be estimated based on the corresponding exospheric density profile. In this study, we estimate the T_{exo} by using an empirical model from Forbes et al. (2008):

$$T_{exo} = 130.7 + 1.53F_{10.7} - 13.5\cos(L_s - 85°), \quad (5)$$

where the $F_{10.7}$ denotes the solar radio flux at a wavelength of 10.7 cm, and L_s represents the solar longitude of Mars. We use the solar parameters provided by the OMNI database near Earth and then calculate the $F_{10.7}$ index at Mars by adjusting for the heliocentric distances of Earth and Mars at the corresponding times. During the periods T_1, T_2, and T_3, T_{exo} are estimated to be 194, 189, and 187 K, respectively.

Thus, we estimate the penetrating H-ENA intensity on the X = 1.6 R_M (Mars radii) plane—corresponding to the bow shock nose, based on the empirical model (Edberg et al., 2008)—within a transverse distance range $d = \sqrt{Y^2 + Z^2}$ from 0 to 1 R_M. This estimation is based on the observed H-ENA intensity (Figure 3) and the corresponding exobase temperature T_{exo}. As an example, the resulting distribution of penetrating H-ENAs during T_3, the interval with the highest observed intensity, is shown in Figure 4a. The penetrating H-ENA intensity decreases with d because of the decreasing exosphere density with increasing distance from Mars. The highest intensity on the dayside reference surface occurs at the subsolar point, reaching 5.3×10^6 s^{-1} cm^{-2}, whereas the lowest intensity is observed near the edge of the reference surface, with a value of 3.4×10^6 s^{-1} cm^{-2}. This means the penetrating intensity is 1.8 to 2.8 times higher than the observed H-ENA intensity (1.9×10^6 s^{-1} cm^{-2}).

From the penetrating H-ENA intensity, we further estimate the penetrating energy flux over the Mars surface (Figure 4b). The energy flux is calculated by multiplying the energy of a single penetrating H-ENA particle $\left(E_k = \frac{1}{2}mV_H^2\right)$ by the penetrating intensity:

$$F_E = E_k \times I_H \times \cos(SZA), \quad (6)$$

where F_E represents the penetrating energy flux over the Mars surface. The penetrating energy from H-ENAs falls in a range of $(0.5-8.1) \times 10^{-3}$ mW/m^2 during this time interval, which is roughly three orders of magnitude lower than the solar ultraviolext radiation on Mars' surface (~3 mW/m^2). Nevertheless, the H-ENAs still contribute nonnegligibly to the atmospheric escape processes on Mars because of their distinct interactions with the Martian atmosphere.

Figures 5a–5b show the penetrating H-ENA intensity and energy change with the SZA. The solid black, blue, and red curves indicate the results during T_1, T_2, and T_3, respectively. Both the penetrating intensity and energy decrease with increasing SZA from 0° to 90° for all time intervals. Additionally, the penetrating H-ENA intensity and energy flux increase from T_1 to T_3, indicating an increased interaction between the solar wind ions, H-ENAs, and Mars' atmosphere.

With the penetrating H-ENA intensity and bulk speed, we construct a test particle Monte Carlo model to simulate their energy degradation and the resulting atmospheric recoils in the Martian atmosphere. The model is analogous to previous atmospheric sputtering models on Mars (e.g., Leblanc et al., 2015, 2018) and is modified from our earlier model of N_2 and CH_4 sputtering escape on Titan (Gu H et al., 2019). The sputtering yields of various species, defined as the average number of escaping atmospheric neutrals produced per incident H-ENA, is computed following the methodology of Gu H et al. (2019). The background atmosphere, composed of CO_2, CO, N_2, O, He, H_2, and H and assumed to be spherically symmetric, is taken from Gu H et al. (2025) for altitudes between 100 and 500 km, representing dayside average conditions under solar median flux. Below 100 km, the mean free path for

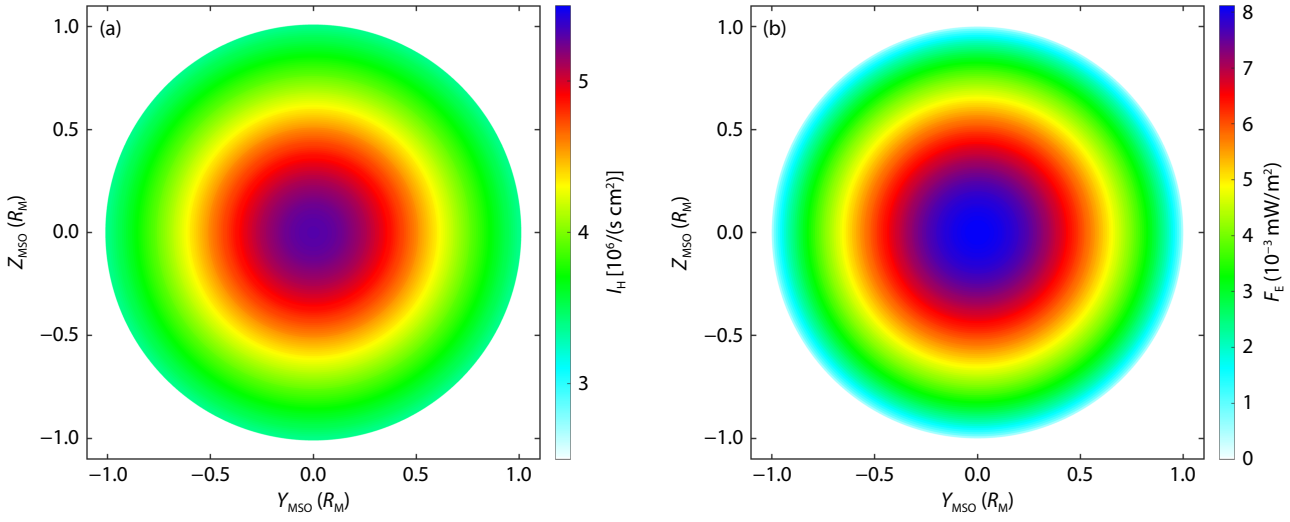

Figure 4. (a) Intensity and (b) energy flux of penetrating H-ENA on the dayside of Mars at the X = 1.6 R_M plane.

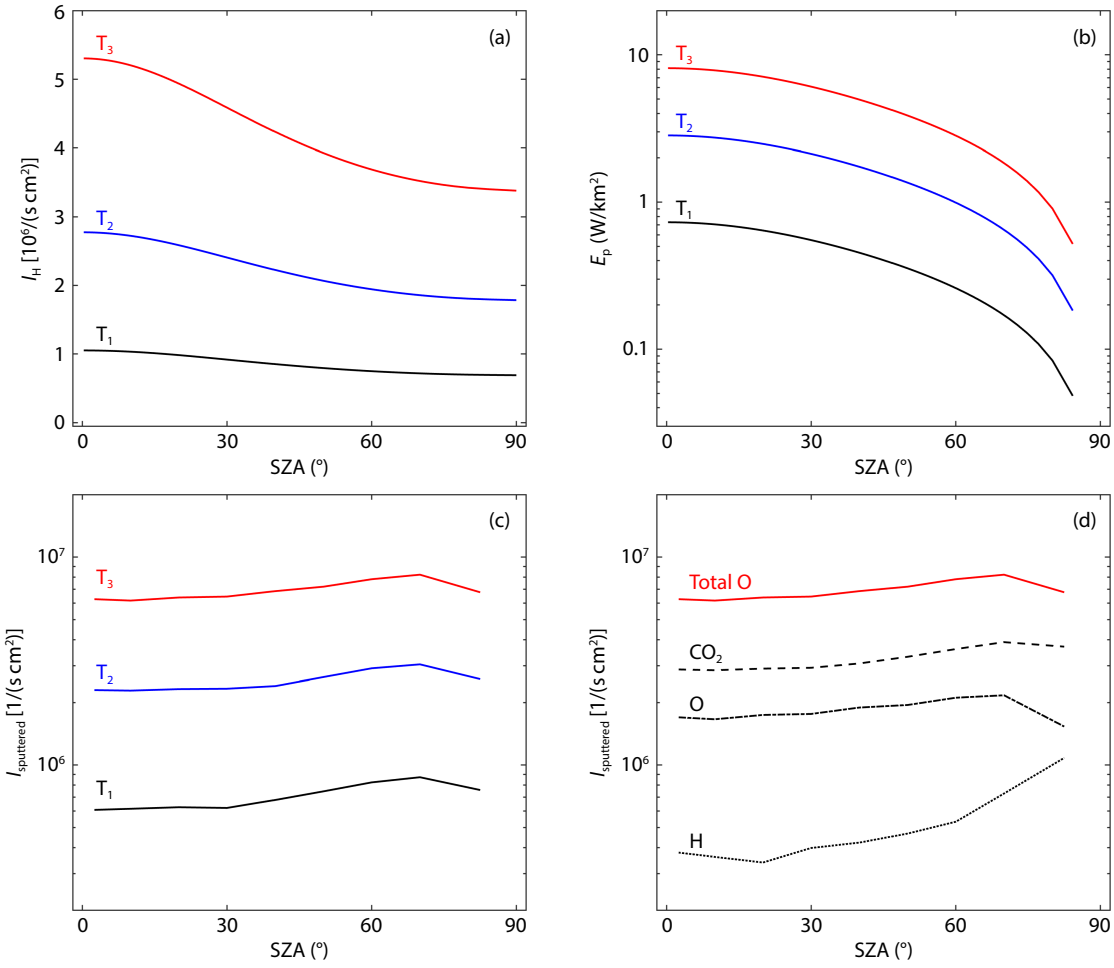

Figure 5. (a) Intensity and (b) energy flux of penetrating H-ENAs and (c) sputtered O intensity as functions of the SZA. The black, blue, and red curves correspond to the time intervals T_1, T_2, and T_3, marked by the yellow shading in Figure 2. (d) Intensity of sputtered total O (the sum of the sputtered intensity of atomic oxygen [O] and twice that of carbon dioxide [CO_2], red curve), CO_2 (dashed black line), O (dashed-dotted black line), and H (dotted line) during T_3.

collisions is sufficiently short that the energy of a typical atmospheric molecule is rapidly degraded to the local thermal level over a length scale of less than 100 m, effectively achieving local thermalization. Above 500 km, the collision probability drops to approximately 1%, indicating that the Martian atmosphere above this altitude has a negligible influence on the computed sputtering yields.

For each H-ENA with a given velocity impacting the atmosphere, its trajectory is tracked step by step, with collisions simulated using a random number generator. Upon collision, the post-collision velocities of both the H-ENA and the ambient atmospheric particles are determined using conservation of momentum and energy while accounting for inelastic energy loss based on the analytic formula of Firsov (1959). The parameterization scheme used for binary collisions, including cross sections and scattering angle distributions, is adapted from Gu H et al. (2020). Trajectory tracking is terminated under two conditions: (1) when the incident H-ENA reaches the lower boundary or its kinetic energy falls below the local escape energy because of successive collisions, or (2) when it reaches the upper boundary, it is considered either lost from the atmosphere or reflected downward elastically, depending on whether its energy exceeds the local escape energy. All recoiling ambient particles generated during the collision cascade are treated using the same procedure as the incident H-ENA. The trajectories of both primary H-ENAs and recoils are fully tracked within the three-dimensional distribution of the Martian atmosphere, which is especially important for accurately evaluating the atmospheric column encountered by particles traveling along limb paths. For each independent model run, 10,000 energetic hydrogen atoms are simulated to ensure statistically robust results. We estimate the atmospheric loss rates driven by ENA-induced sputtering based on the sputtering yields derived from the Monte Carlo simulations, in combination with the known H-ENA flux and bulk speed.

The distribution of total sputtered O escape intensity as a function of the SZA, driven by penetrating H-ENAs, is presented in Figure 5c. The total sputtered O intensity is calculated as the sum of the sputtered intensity of atomic oxygen (O) and twice that of CO_2 given from the model, assuming each sputtered CO_2 molecule contributes two oxygen atoms. The solid black, blue, and red curves represent the results for periods T_1, T_2, and T_3, respectively. Unlike the penetrating H-ENA intensity, the sputtered escape

intensity increases with SZA up to approximately 70°. This trend arises because, at higher SZAs, penetrating H-ENAs travel longer paths through the upper atmosphere before being absorbed. Furthermore, because of geometric effects, the angle between the outward motion of sputtered particles and the incident direction of penetrating H-ENAs is smaller at higher SZAs than at lower SZAs. As a result, sputtered neutral particles at large SZAs have a higher probability of escaping from Mars. As a supplement, Figure 5d shows the sputtered escape intensity for different species: CO_2 (dashed black line), O (dashed-dotted black line), and H (dotted line) during T_3. The differences in their SZA-dependent distributions arise from the distinct altitude profiles of these species in the Martian atmosphere, as well as from variations in their collision processes with penetrating H-ENAs.

By integrating the sputtered escape intensity at the escape surface (200 km higher than Mars surface), the total sputtered escape rate on the dayside of Mars can be calculated, as shown in Table 1. From T_1 to T_3, the sputtered escape increases by an order of magnitude from 5.5×10^{23} s^{-1} to 5.2×10^{24} s^{-1}, reflecting the enhanced intensity and velocity of penetrating H-ENAs.

Table 1. Mars atmospheric sputtering escape rates induced by penetrating H-ENAs to the post-onset of the CME (T_1), the peak ion intensity (T_2), and the post-CME phase (T_3).

Time	η_H (s^{-1})	η_O (s^{-1})	η_{CO_2} (s^{-1})	Total O (s^{-1})
T_1	8.7×10^{22}	3.6×10^{23}	9.3×10^{22}	5.5×10^{23}
T_2	2.4×10^{23}	1.1×10^{24}	4.1×10^{23}	1.9×10^{24}
T_3	4.8×10^{23}	2.5×10^{24}	1.4×10^{24}	5.2×10^{24}

4. Conclusions and Discussion

The MINPA instrument aboard Tianwen-1 offers a unique opportunity to directly observe H-ENAs from the Sun-pointing direction, providing a method for studying penetrating H-ENAs. By analyzing H-ENA data from the MINPA during a CME and an SIR event between December 29, 2021, and January 1, 2022, we examine the temporal sequence of interactions between the solar wind and Mars' atmosphere, including the penetrating H-ENAs and driven sputtered escape, under varying solar conditions.

By integrating H-ENA observations from the MINPA with solar wind ion data from MAVEN/SWIA, we find that the bulk velocity of the H-ENAs closely aligns with that of the solar wind ions. The ratio of H-ENAs to solar wind ion intensity serves as a proxy for variations in exospheric density. During the CME and SIR events, the exospheric density does not immediately increase following the CME impact, nor does it rise concurrently with the surge in solar wind intensity. This delayed response suggests a possible lag in the reaction of the Martian exosphere to changing solar wind conditions.

The penetrating H-ENA intensity and energy flux on the dayside of Mars are estimated by combining H-ENA observations upstream of the bow shock with the classical Chamberlain model. During the study period, the highest intensity of penetrating H-ENAs reaches 5.3×10^{6} s^{-1} cm^{-2}, and the range of the corresponding penetrating energy flux is $(0.5-8.1)\times10^{-3}$ $\frac{mW}{m^2}$, approximately three orders of magnitude lower than the solar ultraviolet radiation measured by MAVEN. Nevertheless, penetrating H-ENAs interact with the atmosphere at different altitudes and through different mechanisms compared with photons (Kallio and Janhunen, 2001), thereby making a distinct and nonnegligible contribution to the dynamics of the dayside Martian atmosphere.

It is important to note that both the penetrating H-ENA intensity and energy flux consider only H-ENAs originating from upstream of the $X = 1.6\ R_M$ plane. The H-ENAs produced by CEX processes occurring in the flanks and downstream of the bow shock are not accounted for in this study. Therefore, the estimated penetrating H-ENA intensity and energy flux should be regarded as lower limits for the dayside Mars atmosphere.

For the sputtered escape, the estimated penetrating H-ENA intensity and energy flux are used as inputs for the sputtered simulation model. During the study period, the total sputtered oxygen escape rate caused by penetrating H-ENAs ranges from 5.5×10^{23} s^{-1} to 5.2×10^{24} s^{-1}, influenced by the intensity and speed of the penetrating H-ENAs. Because of underestimation of the penetrating H-ENA intensity, the sputtered escape rate calculated in this study represents a lower limit.

Considering that Mars was near aphelion during the study period and primarily in a low-speed solar wind region, the penetrating H-ENA flux, energy, and driven sputtered escape rate observed in this study should be regarded as the minimum levels for the Martian year. Despite this, the sputtered escape rate driven by penetrating H-ENAs is slightly higher than that caused by penetrating ions observed by MAVEN over the course of a year, which is 1×10^{24} s^{-1} (Leblanc et al., 2015, 2018). A more comprehensive analysis of penetrating H-ENAs and the resulting sputtered escape rate over the course of a Martian year will provide a more systematic evaluation of the contribution of sputtered escape by penetrating H-ENAs to the total oxygen loss.

Because of the complexity of magnetosheath plasma and its interaction with the neutral exosphere, accurately estimating the contribution of H-ENAs originating from the magnetosheath to the total dayside penetrating H-ENA flux based on high-altitude observations is challenging. Therefore, H-ENA observations at lower altitudes on the dayside of Mars are crucial for accurately estimating the penetrating H-ENA flux and the resulting sputtered escape. Moreover, current H-ENA observations primarily serve as boundary inputs for simulations and do not constrain the collisional interactions between penetrating H-ENAs and the Martian atmosphere. As a result, the interaction process remains poorly defined in the absence of direct observational evidence. Therefore, a more detailed investigation into the dynamics of penetrating H-ENAs and the associated sputtering mechanisms require H-ENA observations at low altitudes—on the order of hundreds of kilometers.

Acknowledgments

The authors acknowledge the China National Space Administration (CNSA), Ground Research and Application System (GRAS), Beijing Aerospace Command and Control Center (BACC), China Academy

of Space Technology (CAST), and Shanghai Academy of Spaceflight Technology for enabling the Tianwen-1 mission and observations of Mars. The authors also acknowledge the entire MAVEN team for providing the SWIA data. This work was supported by the National Natural Science Foundation of China (Grant Nos. 42188101, 42274211, 41974170, 42374184, 42122032, and 41974196), the Chinese Academy of Sciences (Grant Nos. QYZDJSSW-JSC028, XDA15052500, XDA17010301, and XDB41000000), the CNSA (Grant No. D050103), the Specialized Research Fund for State Key Laboratories of China, and the Specialized Research Fund for Laboratory of Geospace Environment of the University of Science and Technology of China. This research was supported by the International Space Science Institute (ISSI) in Bern and Beijing through the ISSI/ISSI-BJ International Team Project titled "Understanding the Mars Space Environment Through Multi-Spacecraft Measurements" (ISSI Team Project No. 23-582 and ISSI-BJ Team Project No. 58).

References

Acuña, M. H., Connerney, J. E. P., Wasilewski, P., Lin, R. P., Anderson, K. A., Carlson, C. W., McFadden, J., Curtis, D. W., Mitchell, D., … Ness, N. F. (1998). Magnetic field and plasma observations at Mars: Initial results of the Mars Global Surveyor mission. *Science*, *279*(5357), 1676–1680. https://doi.org/10.1126/science.279.5357.1676

Barabash, S., Lundin, R., Andersson, H., Brinkfeldt, K., Grigoriev, A., Gunell, H., Holmström, M., Yamauchi, M., Asamura, K., … Thocaven, J. J. (2006). The analyzer of space plasmas and energetic atoms (ASPERA-3) for the Mars Express mission. *Space Sc. Rev.*, *126*(1), 113–164. https://doi.org/10.1007/s11214-006-9124-8

Brain, D. A., McFadden, J. P., Halekas, J. S., Connerney, J. E. P., Bougher, S. W., Curry, S., Dong, C. F., Dong, Y., Eparvier, F., … Seki, K. (2015). The spatial distribution of planetary ion fluxes near Mars observed by MAVEN. *Geophys. Res. Lett.*, *42*(21), 9142–9148. https://doi.org/10.1002/2015GL065293

Carr, M. H. (1986). Mars: A water-rich planet?. *Icarus, 68*(2), 187–216. https://doi.org/10.1016/0019-1035(86)90019-9

Catling, D. C. (2009). Atmospheric evolution, Mars. In V. Gornitz (Ed.), *Encyclopedia of Paleoclimatology and Ancient Environments* (pp. 66–75). Dordrecht, Netherlands: Springer. https://doi.org/10.1007/978-1-4020-4411-3_17

Chaffin, M. S., Fowler, C. M., Deighan, J., Jain, S., Holsclaw, G., Hughes, A., Ramstad, R., Dong, Y. X., Brain, D., … AlMatroushi, H. (2022). Patchy proton aurora at Mars: A global view of solar wind precipitation across the Martian dayside from EMM/EMUS. *Geophys. Res. Lett.*, *49*(17), e2022GL099881. https://doi.org/10.1029/2022GL099881

Chamberlain, J. W. (1963). Planetary coronae and atmospheric evaporation. *Planet. Space Sci.*, *11*(8), 901–960. https://doi.org/10.1016/0032-0633(63)90122-3

Chi, Y. T., Shen, C. L., Cheng, L., Yu, B. K., Miao, B., Wang, Y. M., Zhang, T. L., Zou, Z. X., Xu, M. J., … Du, Y. (2023). Interplanetary coronal mass ejections and stream interaction regions observed by Tianwen-1 and MAVEN at Mars. *Astrophys. J. Suppl. S.*, *267*(1), 3. https://doi.org/10.3847/1538-4365/acd191

Connerney, J. E. P., Espley, J., Lawton, P., Murphy, S., Odom, J., Oliversen, R., and Sheppard, D. (2015). The MAVEN magnetic field investigation. *Space Sci. Rev.*, *195*(1), 257–291. https://doi.org/10.1007/s11214-015-0169-4

Deighan, J., Jain, S. K., Chaffin, M. S., Fang, X. H., Halekas, J. S., Clarke, J. T., Schneider, N. M., Stewart, A. I. F., Chaufray, J. Y., … Jakosky, B. M. (2018). Discovery of a proton aurora at Mars. *Nat. Astron.*, *2*(10), 802–807. https://doi.org/10.1038/s41550-018-0538-5

Edberg, N. J. T., Lester, M., Cowley, S. W. H., and Eriksson, A. I. (2008). Statistical analysis of the location of the Martian magnetic pileup boundary and bow shock and the influence of crustal magnetic fields. *J. Geophys. Res.: Space Phys.*, *113*(A8), A08206. https://doi.org/10.1029/2008JA013096

Fan, K., Yan, L. M., Wei, Y., Zhang, A. B., Kong, L. G., Fränz, M., He, F., Chai, L. H., Yuan, C. J., … Wang, C. (2022). The solar wind plasma upstream of Mars observed by Tianwen-1: Comparison with Mars express and MAVEN. *Sci. China Earth Sci.*, *65*(4), 759–768. https://doi.org/10.1007/s11430-021-9917-0

Firsov, O. B. (1959). A qualitative interpretation of the mean electron excitation energy in atomic collisions. *Sov. Phys. J.*, *36*(9), 1076–1080.

Forbes, J. M., Lemoine, F. G., Bruinsma, S. L., Smith, M. D., and Zhang, X. L. (2008). Solar flux variability of Mars' exosphere densities and temperatures. *Geophys. Res. Lett.*, *35*(1), L01201. https://doi.org/10.1029/2007GL031904

Futaana, Y., Barabash, S., Grigoriev, A., Holmström, M., Kallio, E., son Brandt, P. C., Gunell, H., Brinkfeldt, K., Lundin, R., … Dierker, C. (2006a). First ENA observations at Mars: ENA emissions from the Martian upper atmosphere. *Icarus*, *182*(2), 424–430. https://doi.org/10.1016/j.icarus.2005.09.019

Futaana, Y., Barabash, S., Grigoriev, A., Holmström, M., Kallio, E., son Brandt, P. C., Gunell, H., Brinkfeldt, K., Lundin, R., … Dierker, C. (2006b). First ENA observations at Mars: Subsolar ENA jet. *Icarus*, *182*(2), 413–423. https://doi.org/10.1016/j.icarus.2005.08.024

Futaana, Y., Chaufray, J. Y., Todd Smith, H., Garnier, P., Lichtenegger, H., Delva, M., Gröller, H., and Mura, A. (2011). Exospheres and energetic neutral atoms of Mars, Venus and Titan. *Space Sci. Rev.*, *162*(1), 213–266. https://doi.org/10.1007/s11214-011-9834-4

Galli, A., Wurz, P., Barabash, S., Grigoriev, A., Gunell, H., Lundin, R., Holmström, M., and Fedorov, A. (2006). Energetic hydrogen and oxygen atoms observed on the nightside of Mars. *Space Sci. Rev.*, *126*(1-4), 267–297. https://doi.org/10.1007/s11214-006-9088-8

Galli, A., Wurz, P., Kallio, E., Ekenbäck, A., Holmström, M., Barabash, S., Grigoriev, A., Futaana, Y., Fok, M. C., and Gunell, H. (2008). Tailward flow of energetic neutral atoms observed at Mars. *J. Geophys. Res.: Planets*, *113*(E12), E12012. https://doi.org/10.1029/2008JE003139

Gu, H., Cui, J., Niu, D. D., Wellbrock, A., Tseng, W. L., and Xu, X. J. (2019). Monte Carlo calculations of the atmospheric sputtering yields on Titan. *Astron. Astrophys.*, *623*, A18. https://doi.org/10.1051/0004-6361/201833761

Gu, H., Cui, J., Niu, D. D., He, Z. G., and Li, K. (2020). Monte Carlo calculations of helium escape on Mars via energy transfer from hot oxygen atoms. *Astrophys. J.*, *902*(2), 121. https://doi.org/10.3847/1538-4357/abb6e9

Gu, H., Wu, X. S., Cui, J., Huang, X., Li, W. L., Zhao, J. J., and Li, L. (2025). Atmospheric distribution and escape of odd nitrogen on Mars. *Astron. J.*, *169*(2), 74. https://doi.org/10.3847/1538-3881/ad9c3c

Halekas, J. S., Lillis, R. J., Mitchell, D. L., Cravens, T. E., Mazelle, C., Connerney, J. E. P., Espley, J. R., Mahaffy, P. R., Benna, M., … Ruhunusiri, S. (2015a). MAVEN observations of solar wind hydrogen deposition in the atmosphere of Mars. *Geophys. Res. Lett.*, *42*(21), 8901–8909. https://doi.org/10.1002/2015GL064693

Halekas, J. S., Taylor, E. R., Dalton, G., Johnson, G., Curtis, D. W., McFadden, J. P., Mitchell, D. L., Lin, R. P., and Jakosky, B. M. (2015b). The solar wind ion analyzer for MAVEN. *Space Sci. Rev.*, *195*(1), 125–151. https://doi.org/10.1007/s11214-013-0029-z

Halekas, J. S. (2017). Seasonal variability of the hydrogen exosphere of Mars. *J. Geophys. Res.: Planets*, *122*(5), 901–911. https://doi.org/10.1002/2017JE005306

Holmström, M., Barabash, S., and Kallio, E. (2002). Energetic neutral atoms at Mars 1. Imaging of solar wind protons. *J. Geophys. Res.: Space Phys.*, *107*(A10), SSH 4-1–SSH 4-9. https://doi.org/10.1029/2001JA000325

Jakosky, B. M., Lin, R. P., Grebowsky, J. M., Luhmann, J. G., Mitchell, D. F., Beutelschies, G., Priser, T., Acuna, M., Andersson, L., … Zurek, R. (2015). The *Mars Atmosphere* and *Volatile Evolution* (*MAVEN*) mission. *Space Sci. Rev.*, *195*(1), 3–48. https://doi.org/10.1007/s11214-015-0139-x

Jakosky, B. M., Brain, D., Chaffin, M., Curry, S., Deighan, J., Grebowsky, J., Halekas, J., Leblanc, F., Lillis, R., … Zurek, R. (2018). Loss of the Martian atmosphere to space: Present-day loss rates determined from *MAVEN* observations and integrated loss through time. *Icarus*, *315*, 146–157. https://doi.org/10.1016/j.icarus.2018.05.030

Kallio, E., and Barabash, S. (2001). Atmospheric effects of precipitating energetic hydrogen atoms on the Martian atmosphere. *J. Geophys. Res.: Space Phys.*, *106*(A1), 165–177. https://doi.org/10.1029/2000JA002003

Kallio, E., and Janhunen, P. (2001). Atmospheric effects of proton precipitation in the Martian atmosphere and its connection to the Mars–solar wind

interaction. *J. Geophys. Res.: Space Phys.*, *106*(A4), 5617–5634. https://doi.org/10.1029/2000JA000239

Kallio, E., Barabash, S., Brinkfeldt, K., Gunell, H., Holmström, M., Futaana, Y., Schmidt, W., Säles, T., Koskinen, H., … Dierker, C. (2006). Energetic Neutral Atoms (ENA) at Mars: Properties of the hydrogen atoms produced upstream of the martian bow shock and implications for ENA sounding technique around non-magnetized planets. *Icarus*, *182*(2), 448–463. https://doi.org/10.1016/j.icarus.2005.12.019

Kong, L. G., Zhang, A. B., Tian, Z., Zheng, X. Z., Wang, W. J., Liu, B., Wurz, P., Piazza, D., Etter, A., … Sun, Y. Q. (2020). Mars Ion and Neutral Particle Analyzer (MINPA) for Chinese Mars Exploration Mission (Tianwen-1): Design and ground calibration. *Earth Planet. Phys.*, *4*(4), 333–344. https://doi.org/10.26464/epp2020053

Lammer, H., Chassefière, E., Karatekin, Ö., Morschhauser, A., Niles, P. B., Mousis, O., Odert, P., Möstl, U. V., Breuer, D., … Pham, L. B. S. (2013). Outgassing history and escape of the Martian atmosphere and water inventory. *Space Sci. Rev.*, *174*(1), 113–154. https://doi.org/10.1007/s11214-012-9943-8

Leblanc, F., Modolo, R., Curry, S., Luhmann, J., Lillis, R., Chaufray, J. Y., Hara, T., McFadden, J., Halekas, J., … Jakosky, B. (2015). Mars heavy ion precipitating flux as measured by Mars Atmosphere and Volatile EvolutioN. *Geophys. Res. Lett.*, *42*(21), 9135–9141. https://doi.org/10.1002/2015GL066170

Leblanc, F., Martinez, A., Chaufray, J. Y., Modolo, R., Hara, T., Luhmann, J., Lillis, R., Curry, S., McFadden, J., … Jakosky, B. (2018). On Mars's atmospheric sputtering after MAVEN's first Martian year of measurements. *Geophys. Res. Lett.*, *45*(10), 4685–4691. https://doi.org/10.1002/2018GL077199

Lichtenegger, H., Lammer, H., and Stumptner, W. (2002). Energetic neutral atoms at Mars 3. Flux and energy distributions of planetary energetic H atoms. *J. Geophys. Res.: Space Phys.*, *107*(A10), SSH 6-1–SSH 6-9. https://doi.org/10.1029/2001JA000322

Lillis, R. J., Brain, D. A., Bougher, S. W., Leblanc, F., Luhmann, J. G., Jakosky, B. M., Modolo, R., Fox, J., Deighan, J., … Lin, R. P. (2015). Characterizing atmospheric escape from Mars today and through time, with MAVEN. *Space Sci. Rev.*, *195*(1), 357–422. https://doi.org/10.1007/s11214-015-0165-8

Lillis, R. J., Deighan, J., Fox, J. L., Bougher, S. W., Lee, Y., Combi, M. R., Cravens, T. E., Rahmati, A., Mahaffy, P. R., … Chaufray, J. Y. (2017). Photochemical escape of oxygen from Mars: First results from MAVEN in situ data. *J. Geophys. Res.: Space Phys.*, *122*(3), 3815–3836. https://doi.org/10.1002/2016JA023525

Lindsay, B. G., and Stebbings, R. F. (2005). Charge transfer cross sections for energetic neutral atom data analysis. *J. Geophys. Res.: Space Phys.*, *110*(A12), A12213. https://doi.org/10.1029/2005JA011298

Liu, K., Hao, X. J., Li, Y. R., Zhang, T. L., Pan, Z. H., Chen, M. M., Hu, X. W., Li, X., Shen, C. L., and Wang, Y. M. (2020). Mars Orbiter magnetometer of China's First Mars Mission Tianwen-1. *Earth Planet. Phys.*, *4*(4), 384–389. https://doi.org/10.26464/epp2020058

Schmidt, R. (2003). Mars Express—ESA's first mission to planet Mars. *Acta Astronaut.*, *52*(2-6), 197–202. https://doi.org/10.1016/S0094-5765(02)00157-1

Tang, S. W., Wang, Y., Zhao, H. Y., Fang, F., Qian, Y., Zhang, Y. J., Yang, H. B., Li, C. H., Fu, Q., … Sun, Z. P. (2020). Calibration of Mars Energetic Particle Analyzer (MEPA). *Earth Planet. Phys.*, *4*(4), 355–363. https://doi.org/10.26464/epp2020055

Wang, L. M., Li, L., Li, W. Y., Kong, L. G., Tang, B. B., Ma, J. J., Zhang, Y. T., Xie, L. H., Zhang, A. B., … Galli, A. (2023). Characterizing and removing ultra-violet contamination in ion observations on board Tianwen-1. *Atmosphere, 15*(1), 19. https://doi.org/10.3390/atmos15010019

Yan, G., Zhou, J. S., Li, A., Fu, Z. L., Meng, L. Z., Liu, J. J., and Wang, H. P. (2018). A brief introduction of the first Mars exploration mission in China. *J. Deep Space Explor.*, *5*(5), 399–405. https://doi.org/10.15982/j.issn.2095-7777.2018.05.001

Ye, P. J., Sun, Z. Z., Rao, W., and Meng, L. Z. (2017). Mission overview and key technologies of the first Mars probe of China. *Sci. China Technol. Sci.*, *60*(5), 649–657. https://doi.org/10.1007/s11431-016-9035-5

Zhang, A. B., Kong, L. G., Li, W. Y., Li, L., Tang, B. B., Rong, Z. J., Wei, Y., Ma, J. J., Zhang, Y. T., … Wang, C. (2022). Tianwen-1 MINPA observations in the solar wind. *Earth Planet. Phys.*, *6*(1), 1–9. https://doi.org/10.26464/epp2022014